

# Supplementary Information for

## Burrowing dynamics of aquatic worms in soft sediments

Arshad Kudrolli and Bernny Ramirez

Arshad Kudrolli.

E-mail: [akudrolli@clarku.edu](mailto:akudrolli@clarku.edu)

### This PDF file includes:

- Supplementary text
- Figs. S1 to S7
- Table S1
- Captions for Movies S1 to S5
- Captions for Databases S1 to S5
- References for SI reference citations

### Other supplementary materials for this manuscript include the following:

- Movies S1 to S5
- Databases S1 to S5



## Supporting Information Text

### Effect of Container Thickness

In addition to measuring the dynamics of *L. variegatus* in a water-saturated sediment filled container with  $W_c = 2$  mm shown in Fig. 2 and 3, we also analyzed its dynamics in a wider container with  $W_c = 12.7$  mm, and a cuboid container with  $W_c = 100$  mm, to understand the effect of side wall constraints on the dynamics. Sample trajectories can be found in SI Appendix, Fig. S3A for container with  $W_c = 12.7$  mm, and in SI Appendix, Fig. S2 for the cuboid container. While the worm dynamics was only viewed from one direction for  $W_c = 12.7$  mm and  $W_c = 2$  mm, it was viewed through the top and the side to obtain the trajectory in the cuboid container in 3D.

Then, we used the measured dynamic length  $l_w(t)$  as a function of time to infer the motion out of the projected plane in the case where  $W_c = 12.7$  mm. If the worm moves across the container, essentially in the X-Y measurement plane, then one can expect the worm length to oscillate about its length  $l_w$  because of elongation-contraction of its body. However, if the worm also moves in direction which is substantially out of this plane, its projected length can be expected to be smaller. We have observed that the time over which the worm is much longer than the time scale of longitudinal oscillations  $T_L$ . This fact can be observed in the projected length  $l_w(t)$  in SI Appendix, Fig. S3A corresponding to the trajectory shown in SI Appendix, Fig. S3B. Here, we note that the worm length oscillations around its mean length decreases intermittently as for example where when turns around  $t = 100$  s in this example. Thus, we analyze the data for the transverse undulation amplitude and the worm speed in time intervals where the worm appears to move across the container essentially in the X-Y plane. While, prone to errors in identifying the actual length changes  $\Delta l_w$  and separating them from out of plane transverse oscillations, we found it practically easier to measure the projected shapes, in contrast with piecing together the full shape of the worm from the two projections shown in SI Appendix, Fig. S2.

The measured  $A_T$  corresponding to the container with  $W_c = 12.7$  mm and  $W_c = 2$  mm using various worms and their trajectories listed in SI Appendix, Table S1 are shown in SI Appendix, Fig. S3C. We observe  $A_T$  increases similarly with  $l_w$  in both cases. However, if the worm is not constrained to move in two dimensions (when  $W_c \gg A_T$ ), then its body can be in all three dimensions as can be inferred from orthogonal view of the worm dynamics in cuboid container shown in Fig. S2B,C. I.e., the undulations of the worm are not planar and can be in general be in the two orthogonal directions to the direction of propagation. Thus, while  $B = \sqrt{2}A_T$  because of temporal averaging, if the motion is in a two dimensional plane,  $B = 2A_T$ , if the transverse undulations extend in the two orthogonal directions to the direction of motion of the worm. The extra factor of  $\sqrt{2}$  arises because of the spatial averaging of oscillations in the two orthogonal directions. Using this estimate of  $B$  in estimating the undulating component, we obtain  $U_{cal}$  in case of the worms moving in the container  $W_c = 12.7$  mm container, and plot it against  $v_w$  in SI Appendix, Fig. S3D. Reasonable agreement is observed with dashed line corresponding to  $U_{cal} = v_w$  considering that systematic errors arise in the estimate of the amplitude of peristaltic motion and the worm speed, because only the projected distance in two dimensions is measured in these cases.

### Effect of Sediment Consolidation on Anchoring

We examined the effect of sediment consolidation on the worm dynamics by performing experiments with *L. variegatus* confined to a shallow sediment layer schematically represented in SI Appendix, Fig. S4A. This container is the same as the one used to measure the dynamics of the worm in water shown in Fig. 2B, where the worm is constrained to move between two parallel plates separated



by  $H_c = 2 \text{ mm}$  while being immersed in a larger container filled with water. The medium is not laterally constrained at the sides. Thus, the grains can freely exchange positions with the water in the container in which it is placed to maintain overburden  $P$  to be essentially zero.

Snapshots of the projected worm body is shown over a total time interval  $T = 20 \text{ s}$ , and at  $\Delta t = 200 \text{ ms}$  time intervals. Measuring the speed of the worm over this time interval, we find  $v_w = 0.92 \text{ mm s}^{-1}$ . We observe that the same worm moves forward in a much narrower path compared with swimming in water, where it measured to swim with speeds ranging between  $0.3 \text{ mm s}^{-1}$  and  $0.4 \text{ mm s}^{-1}$ . Thus, the measured speed is systematically higher in the granular medium even in the absence of overburden pressure.

Next, we plot  $K_L(t)$  to find the worm length oscillations in SI Appendix, Fig. S4C, and  $K_v(t)$  to find any velocity oscillations associated with peristaltic motion in SI Appendix, Fig. S4D. While a clear peak is observed in  $K_L(t)$  at  $t = 5 \text{ s}$ , we do not observe a clear peak at the same period or half the period in  $K_v(t)$ . This appears to indicate that while the worm performs periodic elongation-contraction of its body, it cannot effectively anchor itself in the medium to take advantage of this stroke to perform peristaltic motion. As shown quantitatively in SI Appendix, Fig. S4B, while the path is narrower in this shallower system compared to swimming in water, it is wider compared to the path followed deeper in the sediment bed. This is a consequence of the fact that the sediments are not as well consolidated as when they are under significant confining pressure due the weight of the grains above. Further evidence of the narrowing of the path with depth can be seen in the trajectories that go from near the bed surface to deep within shown in Fig. S2C in case of *L. variegatus*, and SI Appendix, Fig. S7A in case of *E. fetida*.

Then estimating the undulation speed assuming  $\xi_r = 6$ , we find  $U_{und} = 0.94 \text{ mm s}^{-1}$ , which essentially matches the measured speed of the worm through the speed. Similar behavior was also observed with the two other worms tested where the measured speeds was greater than that measured when only water was present, and evidence of peristaltic motion was absent. This data is plotted in Fig. 5 along with speeds measured and calculated under other conditions, and similar level of agreement is observed.

Thus, we surmise that because the granular medium is not laterally confined and  $P \approx 0$ , the grains are pushed out by the undulating worm. This does not allow the worm surface to grip the surrounding grains which can simply roll away. This absence of anchoring is borne out not only in the lack of signature of a peak at  $T_L/2$  in  $K_v(t)$ , but also in the estimate of the calculated worm speeds in comparison to the measured speed. This fact leads to an important conclusion on a need for the dual longitudinal and transverse strokes of the worm. While peristaltic motion may be very effective in moving the worm through well consolidated granular medium, it is not effective in moving the worm near the surface of the sediment bed. Here, the fact the worm can undulate its body transverse allows it to continue to push against the water layer above the bed, but also the loose sediment itself. Because the drag and drag anisotropy is greater in the sediments – as discussed in SI Appendix, Drag Measurements and SI Appendix, Fig. S6 – allows the worm to power through the loosely consolidated surface layers to the deeper layers where peristaltic motion becomes more effective with increasing overburden pressure.

## Worm-Body Orientation Correlations

We calculate the orientation correlation function  $C(s) = \langle \hat{t}(s) \cdot \hat{t}(0) \rangle$ , where  $\hat{t}(s)$  is a unit tangent vector to the body at arc distance  $s$  from the head as shown in SI Appendix, Fig. S5A, and  $\langle \dots \rangle$  corresponds to averaging configurations observed over time. This quantity is used to understand the overall shape of the worm in relation to that of a persistent random walk. According to the



worm-like chain (WLC) model, a continuous flexible isotropic rod is considered to adopt a curved conformation at finite temperature and linear rigid rod conformation at zero temperature (1). In that case, the orientation correlation function  $C_{WLC}(s)$  at arc distance separation  $s$  is given by

$$C_{WLC}(s) = \langle \hat{t}(s) \cdot \hat{t}(0) \rangle = e^{-s/P} \quad [S1]$$

where  $P$  is the persistence length of the rod.

We plot  $C(s)$  in the two mediums in SI Appendix, Fig. S5B as a function of  $s$  scaled by  $l_w$  corresponding to example shown in Fig. 2. We observe that  $C(s)$  decays differently than  $C_{WLC}(s)$  given by Eq. S1. Matching the initial slope, we find  $P$  to be greater than  $l_w$ , but systematic deviations arise for  $s > 0.2$ . Trying alternative fitting functions, we have found

$$C_{Cosine}(s) = \frac{1}{2}(\cos(2\pi s/s_o) + 1), \quad [S2]$$

with  $s_o = 3.3l_w$  to give a description of the initial decay of the correlation (see SI Appendix, Fig. S5B) in case of water over a larger range of  $s$ . The decay of  $C(s)$  is observed to be even slower in the sediment case. Coupled with the observation that  $A_T/l_w \ll 1$ , we conclude that the worm can be considered as undulating about a linear body shape.

## Drag Measurements

We performed experiments with a thin cylindrical rod to measure the drag anisotropy experienced by a worm in the sedimented medium while moving its body perpendicular and parallel relative to its cylindrical axis. The apparatus is schematically shown in SI Appendix, Fig. S6A, and is similar to the one used in Ref. (2). It consists of a rod composed of Polyethylene with diameter  $D_r = 3$  mm and length  $L_r = 80$  mm moving parallel and perpendicular to its axis while attached to a 1 mm thin long arm at the end of a torsional strain gage. The contribution of the thin arm to the drag in the medium is subtracted away by performing a complementary series of experiments with the arm alone to then find the drag corresponding to the rod in the perpendicular and parallel orientations. This setup allows us to measure drag acting on the rod down to  $5 \mu\text{N}$ .

SI Appendix, Figure S6B shows the measured drag per unit length of a rod parallel  $F_{\parallel}$  and perpendicular  $F_{\perp}$  to the direction of motion as a function of speed  $U$  in the same granular medium used to make observations with *L. variegatus*. The range of speeds  $U$  probed is estimated based on the speed of the worm  $v_w$  through the medium, and the depths  $z$  probed correspond to the typical depths where the speed measurements are performed. One observes that  $F_{\perp}$  is systematically higher than  $F_{\parallel}$  over the range of speeds measured and increases sublinearly with speed in both directions. Plotting the ratio  $F_{\parallel}$  versus  $F_{\perp}$  in Fig. S6C, we observe that they increase together linearly. By fitting to the data to a line, we find the drag anisotropy  $\xi_r$  from the slope of the line. By varying the depth of the rod  $z$ , we find an overall increase in drag, consistent with previous measurements on drag experienced by a sphere in the same medium (2). From the fits to data sets at the two depths, we find the drag anisotropy  $\xi_r = 5$  with  $R^2 = 0.98$  and  $\xi_r = 7$  with  $R^2 = 0.91$  at  $z = 5$  cm and 11 cm, respectively. To simplify the analysis, we use the average  $\xi_r = 6$ , while estimating its effect on  $v_w$ .

Further, we obtain the effective viscosity  $\eta_e$  experienced using the measured rod drag in the perpendicular orientation using (3),

$$F_{\perp} = \frac{4\pi\eta_e L_r U}{1/2 - \ln(L_r/D_r)}.$$



We observe from SI Appendix, Fig. S6D that  $\eta_e$  decreases with speed, and thus the medium is shear thinning. Further, this decrease can be captured by a power-law fit to the function  $\eta_e = \eta_o(U_o/U)^\beta$ , with  $\eta_o = 4.0$  at  $U_o = 1 \text{ mm s}^{-1}$  and  $\beta = 0.63$ .

To understand the relative contribution of inertia and viscous forces in the medium to the rheology, we evaluate the inertial number  $I$  and viscous number  $J$  appropriate for moving bodies (3, 4) given by

$$I = \frac{U d_g}{D \sqrt{P/\rho_g}}, \quad [\text{S3}]$$

and

$$J = \frac{\eta_f U}{D P}, \quad [\text{S4}]$$

where,  $\eta_f$  is the viscosity of water at 24°C,  $D$  is the effective length scale over which medium is sheared by the moving body. In case of rods moving through medium with similar sized grains, we assume  $D = D_r + d_g$ . Then, the Stokes number  $\text{St} = I^2/J$  can be used to evaluate the relative importance of inertia and viscosity for the given medium. Using Eq. S3 and Eq. S4, we have

$$\text{St} = \frac{\rho_g d_g^2}{\eta_f D^3}. \quad [\text{S5}]$$

Considering  $\rho_g \sim 10^3 \text{ kg m}^{-3}$ ,  $\eta_f \approx 10^{-4} \text{ Pa s}$ ,  $d_g \approx 10^{-3} \text{ m}$ , and  $D \approx 4 \times 10^{-3} \text{ m}$ , we have  $\text{St} \sim 2 \times 10^8 \gg 1$ , independent of moving body speed and depth, even as  $I$  and  $J$  grow with speed. Now, apply this analysis to the thinner *L. variegatus*, where  $D \sim d_g$ , it can be noted that we still have  $\text{St} \gg 1$ .

Thus, the system is in the high Stokes regime where grain inertia dominates compared with the viscosity of the fluid component, and the appropriate law (2) which describes the effective friction  $\mu_e$  is of the form

$$\mu_e = \mu_o + k I^n \quad [\text{S6}]$$

where,  $\mu_o$ ,  $k$  and  $n$  are material dependent constants. This effective friction  $\mu_e$  corresponds to the ratio of the drag encountered and the weight of the sediments acting on the moving body, can be evaluated from the rod drag using

$$\mu_e = \frac{F_\perp}{(\rho_g - \rho_f) g z L_r d_r}. \quad [\text{S7}]$$

SI Appendix, Figure S6E shows a plot of  $\mu_e$  versus  $I$ , and observe that it increases rapidly as inertial effects grow. We also observe that Eq. S6 describes the data with  $\mu_o = 0.8$ ,  $k = 38 \pm 3$ ,  $n = 0.63$ . The large value of  $\mu_o$  may seem surprising considering that the coefficient of friction between hydrogel grains is 0.03 (5). However, it should be noted that this value corresponds to not only the friction between the moving body and the grains, but also the dilatancy. This dilatancy is associated with the fact that the grains have to move around the body which exerts force normal to the direction of motion, but also in the direction of motion due to the circularity of the rod crosssection (6). This importance of the geometry of the medium flow around the body is also important to the fact that the rod drag encountered in the direction parallel to its axis is different and lower compared to the direction perpendicular to its axis.



**Earthworm Dynamics.** SI Appendix, Table S1 lists the properties of *E. fetida* used to obtain the strokes and locomotion speeds in the sediments. These earthworms are more than twice as long and wide on average as *L. variegatus*, and also have hair like projections called setae used for anchoring on substrates, similar to chaetae in the California blackworms (7). We performed experiments with the same water-saturated granular hydrogel medium but with larger containers with  $L_c = 500$  mm,  $H_c = 300$  mm and  $W_c = 28$  mm to account for the fact that the worms were larger, and greater distance are required to get a good read on their average speeds. Behaviorally, these worms are less dynamic, preferring to stay in a dark place or move to the bottom or a corner of the container, and stay there for long periods of time. Because their natural habitat appears to be moist soil, they were maintained in a container filled with mud and compostable organic matter as a food source. But these worms are known to survive heavy rains which result in flooding and water-logged ground. Indeed, we found that they survived over days when left in a water tank with or without the sediment bed.

When a *E. fetida* specimen was picked and placed in an observation container containing sediments immersed in water, it stayed in place typically for few minutes or even longer before moving, unlike *L. variegatus* which were observed to almost always immediately move and explore the container after being dropped in it. For this reason, it was difficult to perform experiments with thinner containers to further constrain the strokes to two dimensions. As in the case of *L. variegatus*, we used the measured length of the worm as a function of time to infer when the worm were moving across the visualization plane to minimize systematic errors due to out of plane component of motion.

In SI Appendix, Fig. S7A, we show *E. fetida* corresponding to Worm number E3 and Run Number S1 listed in SI Appendix, Table S1, as it moves from near the bed surface toward the bottom of the container. One can observe that the path becomes narrower as the earthworm moves further down because of the increased confinement due to weight of the grains above. The measured length  $l_w$  is then shown over the  $T = 40$  s time interval plotted. One observes that worm appears shorter due to out of plane motion while turning during the first half of the time period plot. We therefore use a 20 second time interval corresponding to the second of the full trajectory shown to find its speed and the contribution of the peristaltic and transverse undulatory motion. We then use  $K_L$  plotted in Fig. 6C to find the dominant time scales  $T_L$ , and then use  $K_T$  plotted in SI Appendix, Fig. S7C to find  $T_T$ .



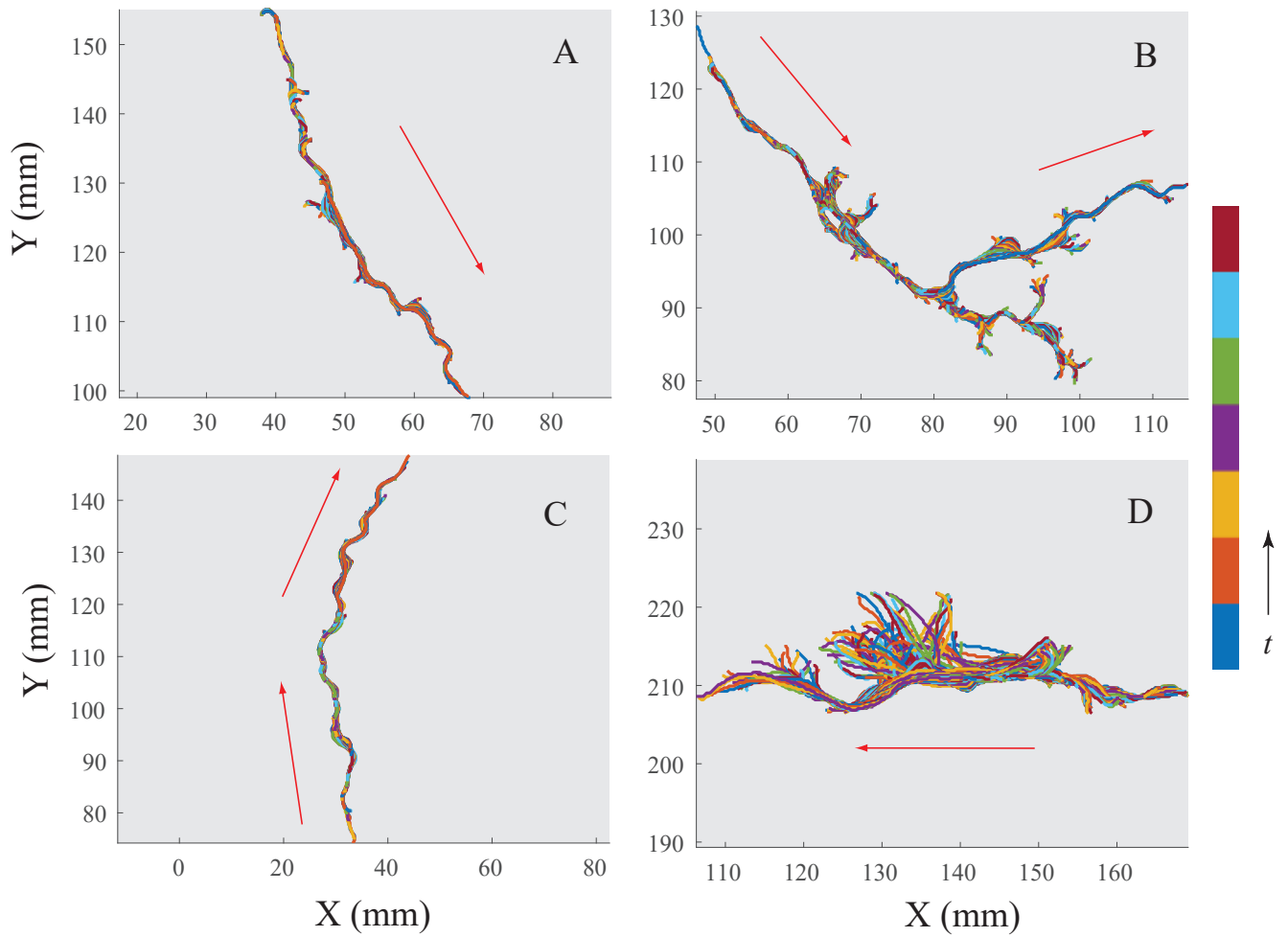


**Fig. S1.** Magnified views of *L. variegatus* burrowing down (A), stopping, moving backwards, and turning (B), burrowing up (C), and moving near the surface (D) corresponding to the example shown in Figure 1D. Arrows indicate the direction of net travel. Higher time resolution is shown as well with images taken at 5 frames per second ( $\Delta t = 200$  ms). The arrows indicate the direction of travel. The line colors repeat in the same sequence over the different colors shown in the color bar. The time  $t$  varies between 80 s and 100 s in (A), 100 s and 180 s in (B), 480 s and 500 s in (C), and 960 s and 1000 s in (D). ( $H_c = 22.2$  cm,  $L_c = 21.5$  cm, and  $W_c = 1.27$  cm.)



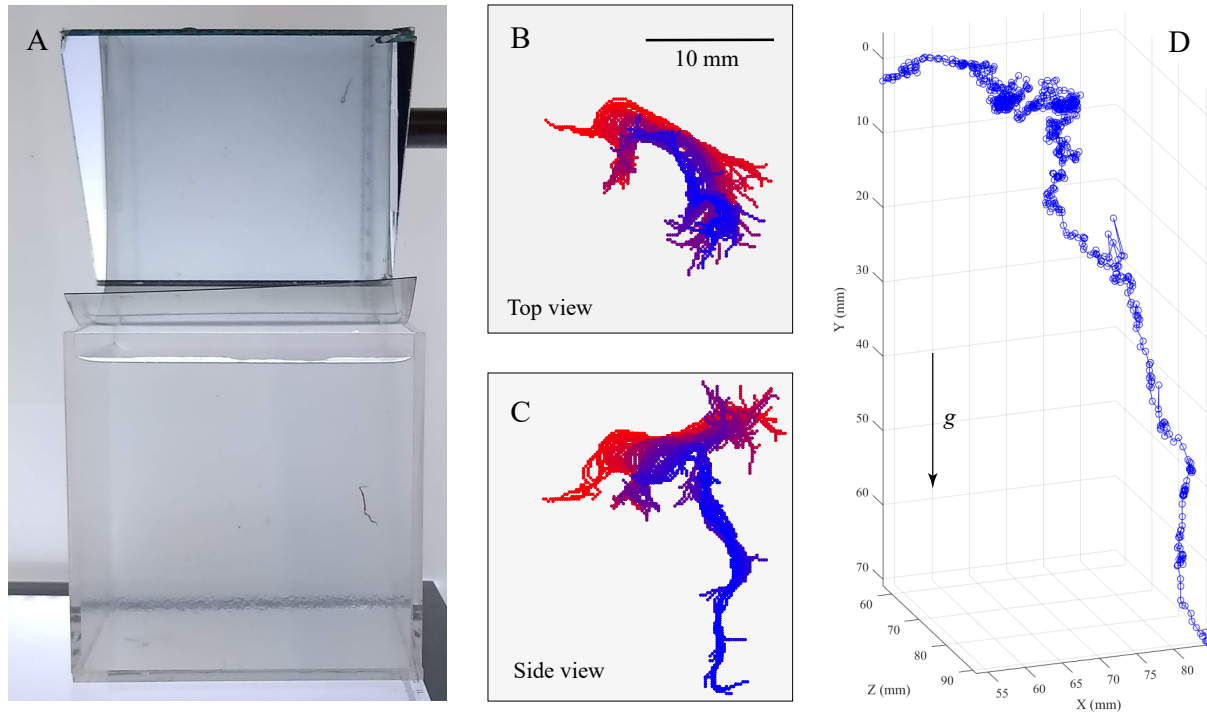


**Fig. S2.** (A) Image of the experimental system used to visualize *L. variegatus* in 3D in a cubical container filled with a transparent sediment bed. ( $H_c = 10$  cm,  $L_c = 10$  cm, and  $W_c = 10$  cm.) A worm can be seen through the transparent side wall and in the mirror above. (B,C) Projected shapes of the worm as viewed from the top (B) and side (C) at  $\Delta t = 1$  s time intervals over total time  $T = 100$  s. The worm is observed to move near the sediment surface for 75 s before burrowing down rapidly. (D) The corresponding trajectory of the worm's center of mass in 3D. The data is plotted with six times higher time resolution  $\Delta t = 167$  ms in (D) compared with the snap shots shown in (B,C). The worm is observed to behave similarly as in the thinner containers shown in Figure 1D and Figure S1, with slower speeds ( $v_w \approx 0.53$  mm/s) observed while moving above the bed surface with greater lateral motion of its body compared to when it burrows into the bed where it moves faster ( $v_w \approx 2.51$  mm/s).



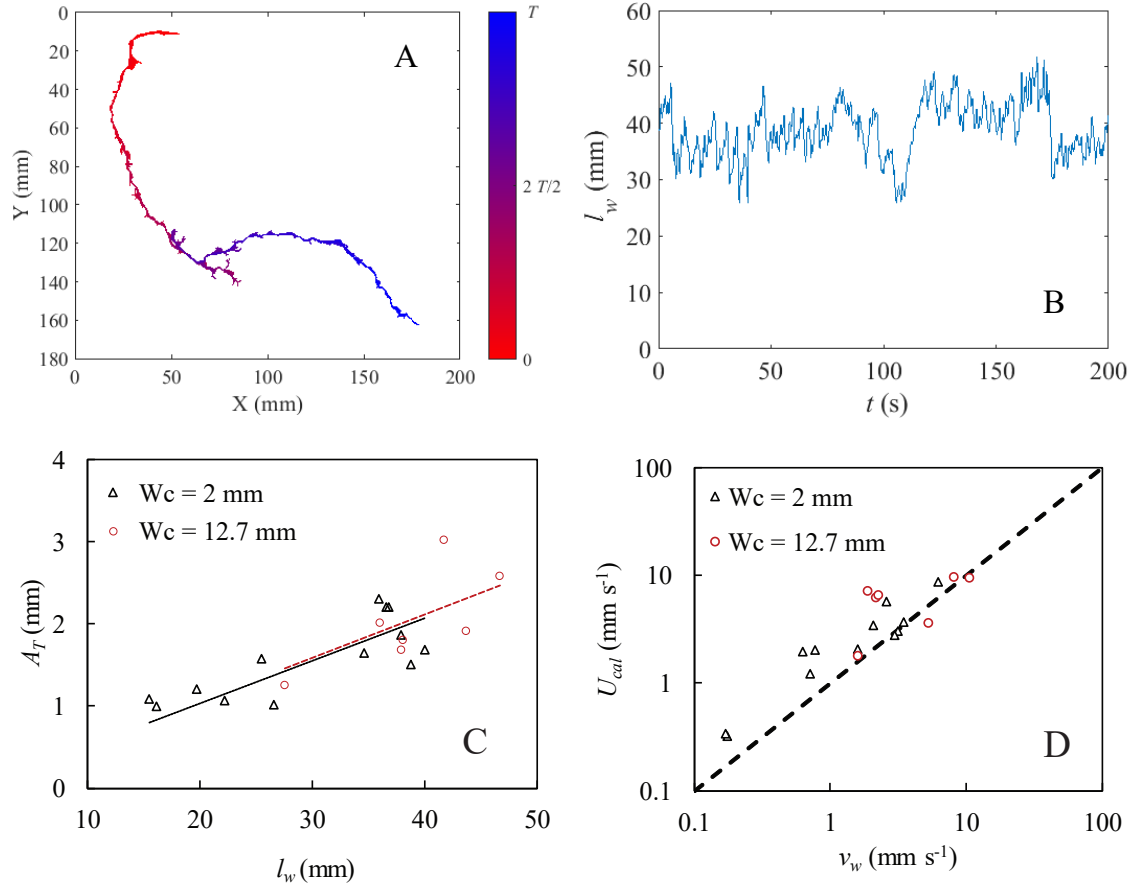


**Fig. S3.** Trajectory of *L. variegatus* ( $l_w = 42.4$  mm) as it burrows down from the top surface into a corner of the  $W_c = 12.7$  mm wide container over  $T = 200$  s (A), and its corresponding projected length  $l_w$  (B). By using time intervals where the length oscillations occur over the longest  $l_w$  recorded, we infer time durations when the worm is essentially moving across the recorded plane. In this example, such a time duration corresponds time between  $t = 120$  s and 160 s. (C) The measured mean transverse amplitude  $A_T$  as a function of the mean lengths  $l_w$  using various worms listed in SI Appendix, Table S1. (D) The calculated speeds are consistent with the measured speeds of the worm in the two different containers. The dashed line has slope 1.



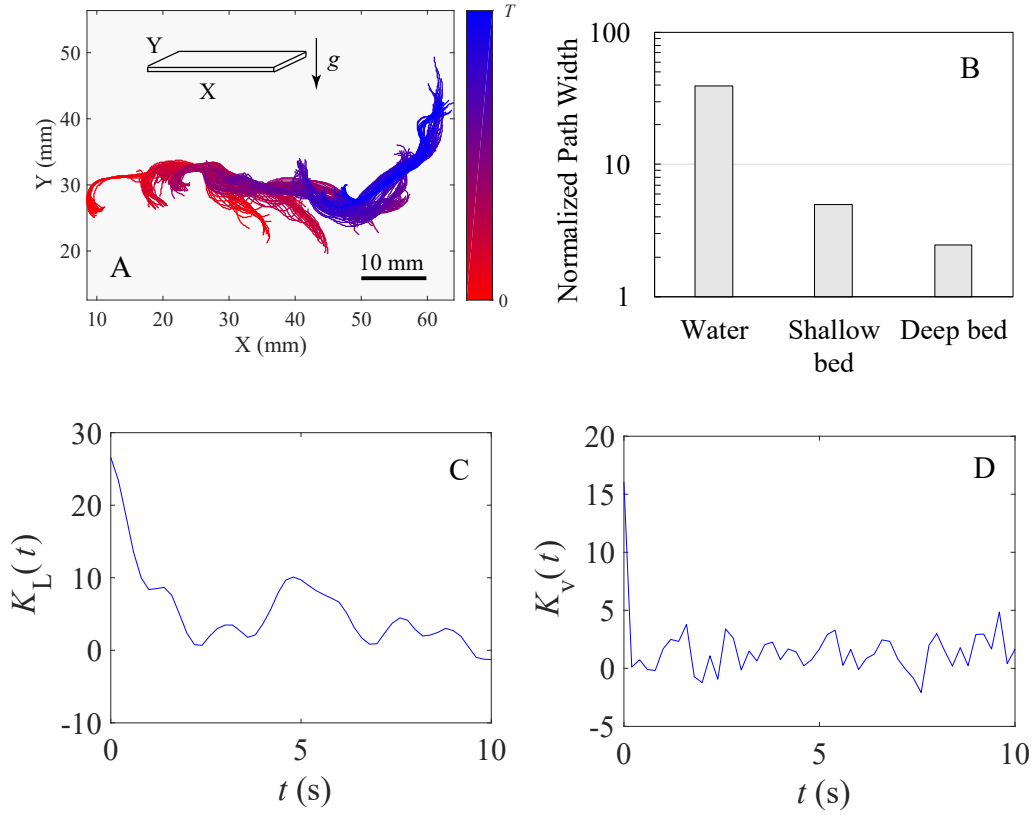


**Fig. S4.** (A) Trajectory of *L. variegatus* confined to a shallow sediment layer between parallel plates ( $H_c = 2$  mm). The relative orientation of the coordinates and gravity is shown schematically in the inset. The grains are not confined laterally in the container and can move away easily when pushed by the body of the worm. Thus, the overburden pressure confining the grain is effectively zero. (B) The width of path followed by the worm normalized by its diameter in the shallow layer as shown in (A) compared with width of the same worm when the sediments are removed and when only water is present. The worm path is significantly narrower in the shallow sediment layer. However, the path still narrower in a deeper bed due to the overburden pressure of the grains. (C)  $K_L(t)$  shows a peak due to elongation and contractions of the worm at approximately  $t = 5$  s. (D) The corresponding  $K_v(t)$  does not show clear peaks demonstrating a lack of peristaltic motion and anchoring. The data corresponds to Worm Number L11 in SI Appendix, Table S1.



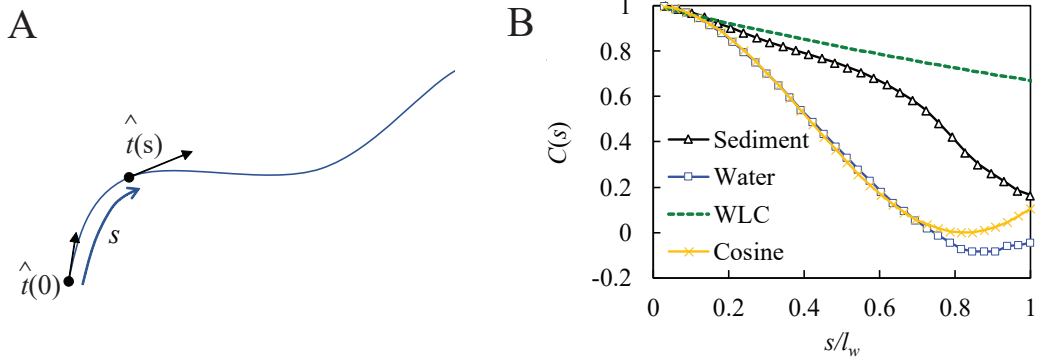


**Fig. S5.** (A) The unit tangent vector  $\hat{t}$  to the worm body corresponding to the worm's head and at arc distance  $s$  from the head along its body. (B) The angle correlation function  $C(s)$  in the two mediums compared with the exponential form corresponding to the WLC model in Eq. S1 with  $P = 2.5 l_w$  to match the initial decay. A fit to a cosine form is also shown (see text).



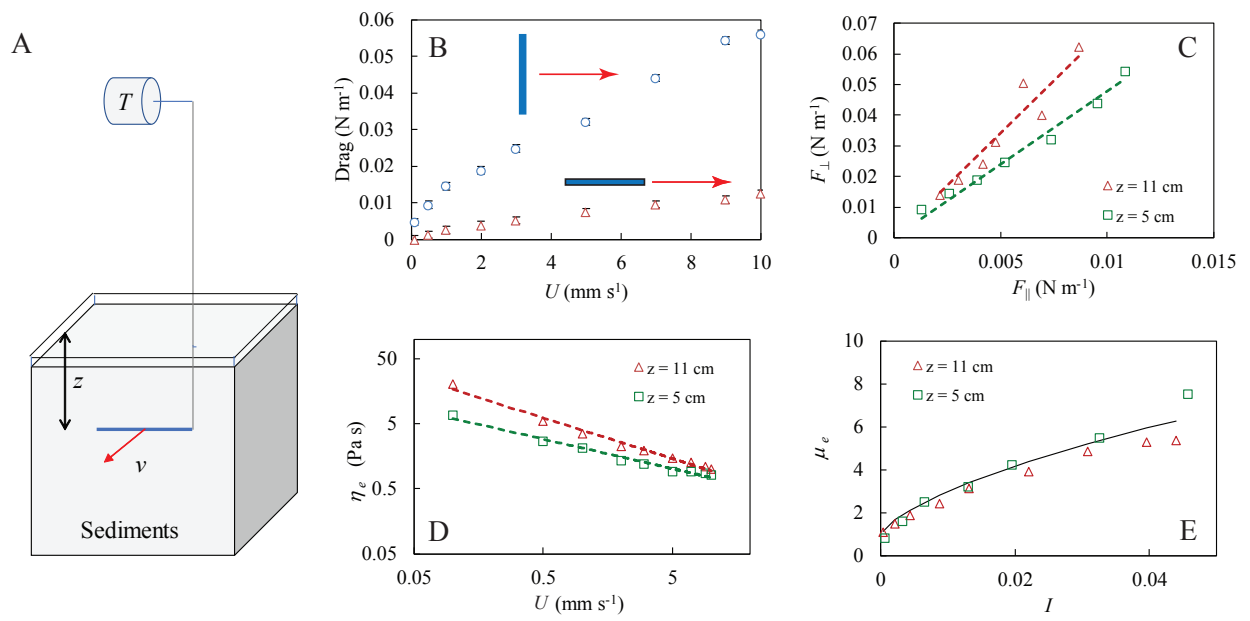


**Fig. S6.** (A) Schematic of the experimental apparatus used to measure the drag acting on a rod in the sediment bed. The rod is moved relative to the medium by placing the container on a computer controlled translating stage which is moved with velocity  $v$  either parallel or perpendicular to the rod axis. (B) The drag  $F_{\perp}$  and  $F_{\parallel}$  of a rod measured perpendicular and parallel to its axis as a function of speed ( $z = 5$  cm). (C)  $F_{\perp}$  versus  $F_{\parallel}$  measured at two different depths. The slope corresponds to the anisotropy of drag  $\xi_r$ . (D) The effective viscosity  $\eta_e$  versus drag speed at  $z = 5$  and 11 cm. The lines corresponds to a power-law fit with exponent  $\beta = 0.46$  and  $\beta = 0.63$ , respectively. (E)  $\mu_e$  versus  $I$  is observed to increase rapidly as inertial effects grow. The data is described by Eq. S6 with  $\mu_o = 0.8$ ,  $k = 38 \pm 3$ , and  $n = 0.63$ .



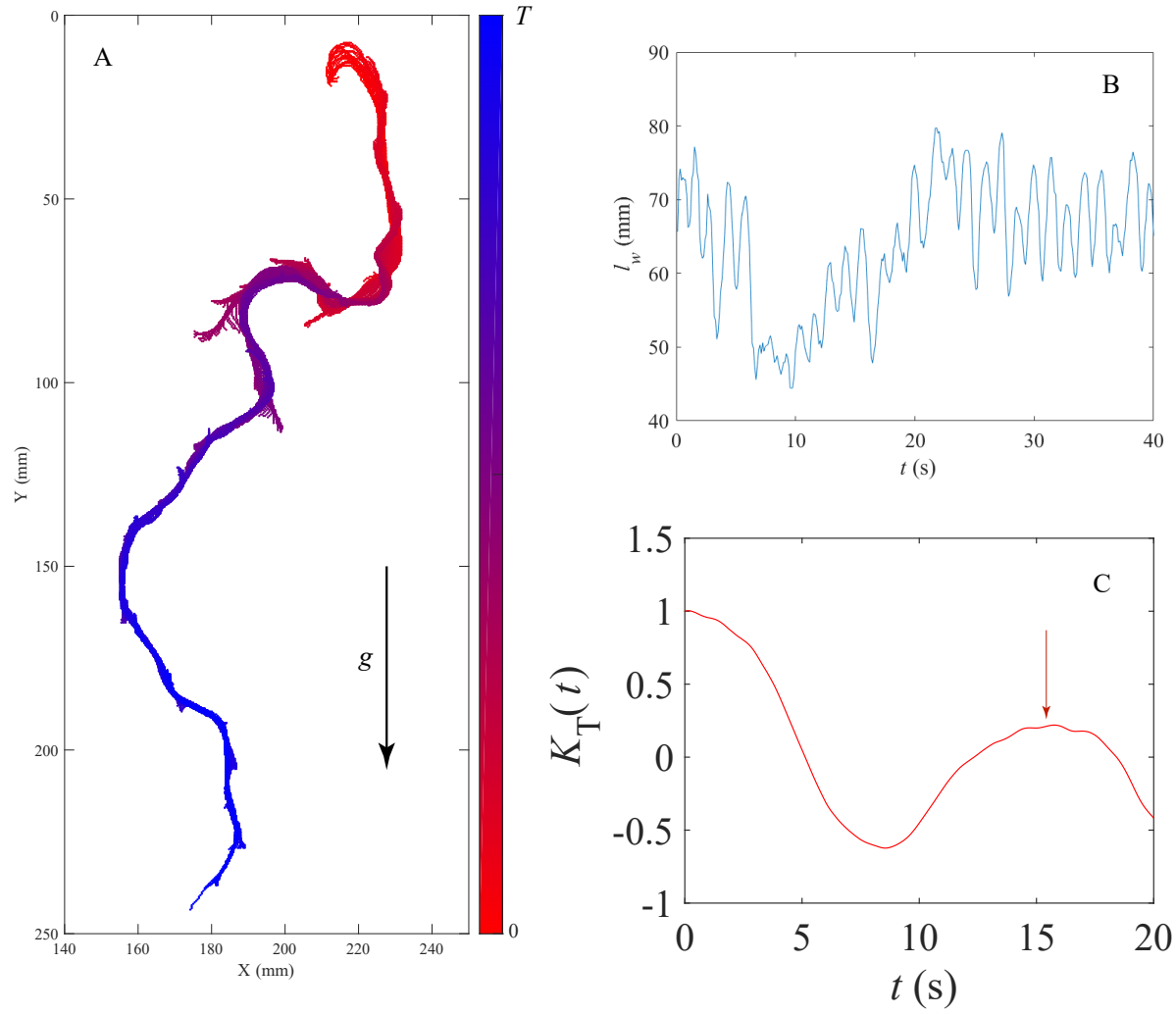


**Fig. S7.** (A) Trajectory of *E. fetida* of length  $l_w = 68.6$  mm as it moves from near the bed surface to the bottom of the container filled with water-saturated granular hydrogels beads over time  $T = 40$  s. The data corresponds to Worm Number E3 and Run Number S1 in SI Appendix, Table S1. (B) The length of the worm over the same time period  $T$ . The projected length is observed to decrease over time  $t = 5$  s to 20 s when the worm turns, rather than move straight down. (C)  $K_T$  corresponding to the last half of the trajectory shows a peak corresponding to  $T_T$ .



**Table S1.** List of various worms and the containers in which their speeds were measured. S and W in run number refer to sediment medium and water, respectively, in which the speeds are measured. The error in length measurements is  $\pm 3\%$ , and the error in speed measurements is  $\pm 5\%$ .

Species	Worm Number	Run Number	Length $l_w$ (mm)	Speed $v_w$ (mm/s)	Container ( $L_c \times H_c \times W_c$ ) (mm)
<i>L. variegatus</i>	L1	S1	38.8	3.14	Quasi-2D ( $155 \times 164 \times 2$ )
<i>L. variegatus</i>	L1	S2	36.8	6.2	Quasi-2D ( $155 \times 164 \times 2$ )
<i>L. variegatus</i>	L1	S3	35.9	2.66	Quasi-2D ( $155 \times 164 \times 2$ )
<i>L. variegatus</i>	L2	S1	36.6	0.63	Quasi-2D ( $155 \times 164 \times 2$ )
<i>L. variegatus</i>	L2	S2	37.9	1.6	Quasi-2D ( $155 \times 164 \times 2$ )
<i>L. variegatus</i>	L3	S1	19.7	0.77	Quasi-2D ( $155 \times 164 \times 2$ )
<i>L. variegatus</i>	L4	S1	25.5	0.71	Quasi-2D ( $155 \times 164 \times 2$ )
<i>L. variegatus</i>	L5	S1	26.6	3.47	Quasi-2D ( $155 \times 164 \times 2$ )
<i>L. variegatus</i>	L6	S1	15.5	0.175	Quasi-2D ( $155 \times 164 \times 2$ )
<i>L. variegatus</i>	L6	S2	16.1	0.17	Quasi-2D ( $155 \times 164 \times 2$ )
<i>L. variegatus</i>	L7	S1	22.2	2.07	Quasi-2D ( $155 \times 164 \times 2$ )
<i>L. variegatus</i>	L8	S1	34.6	2.6	Quasi-2D ( $155 \times 164 \times 2$ )
<i>L. variegatus</i>	L9	S1	40	2.98	Quasi-2D ( $155 \times 164 \times 2$ )
<i>L. variegatus</i>	L10	W1	17	0.28	Quasi-2D ( $150 \times 2 \times 146$ )
<i>L. variegatus</i>	L11	W1	27.1	0.3	Quasi-2D ( $150 \times 2 \times 146$ )
<i>L. variegatus</i>	L11	W2	27.1	0.41	Quasi-2D ( $150 \times 2 \times 146$ )
<i>L. variegatus</i>	L11	W3	27.1	0.42	Quasi-2D ( $150 \times 2 \times 146$ )
<i>L. variegatus</i>	L12	W1	27.4	0.36	Quasi-2D ( $150 \times 2 \times 146$ )
<i>L. variegatus</i>	L13	W1	34.6	0.08	Quasi-2D ( $150 \times 2 \times 146$ )
<i>L. variegatus</i>	L14	W1	39.0	0.45	Quasi-2D ( $150 \times 2 \times 146$ )
<i>L. variegatus</i>	L15	W1	16.1	1.1	Cuboid ( $100 \times 100 \times 100$ )
<i>L. variegatus</i>	L16	W1	26.3	0.057	Cuboid ( $100 \times 100 \times 100$ )
<i>L. variegatus</i>	L17	S1	46.7	2.58	Quasi-2D ( $215 \times 222 \times 12.7$ )
<i>L. variegatus</i>	L18	S1	36	2.01	Quasi-2D ( $215 \times 222 \times 12.7$ )
<i>L. variegatus</i>	L19	S1	38.1	1.8	Quasi-2D ( $215 \times 222 \times 12.7$ )
<i>L. variegatus</i>	L20	S1	22.0	6.28	Quasi-2D ( $215 \times 222 \times 12.7$ )
<i>L. variegatus</i>	L21	S1	27.6	1.25	Quasi-2D ( $215 \times 222 \times 12.7$ )
<i>L. variegatus</i>	L22	S1	43.7	1.91	Quasi-2D ( $215 \times 222 \times 12.7$ )
<i>L. variegatus</i>	L23	S1	37.9	1.68	Quasi-2D ( $215 \times 222 \times 12.7$ )
<i>L. variegatus</i>	L24	S1	42.4	1.59	Quasi-2D ( $215 \times 222 \times 12.7$ )
<i>L. variegatus</i>	L11	S1	27.1	0.92	Quasi-2D ( $150 \times 2 \times 146$ )
<i>L. variegatus</i>	L12	S1	27.4	0.62	Quasi-2D ( $150 \times 2 \times 146$ )
<i>L. variegatus</i>	L13	S1	34.6	0.063	Quasi-2D ( $150 \times 2 \times 146$ )
<i>E. fetida</i>	E1	S1	95	0.75	Quasi-2D ( $500 \times 300 \times 28$ )
<i>E. fetida</i>	E2	S1	80.6	3.3	Quasi-2D ( $500 \times 300 \times 28$ )
<i>E. fetida</i>	E2	S2	78.2	3.2	Quasi-2D ( $500 \times 300 \times 28$ )
<i>E. fetida</i>	E3	S1	68.6	7.3	Quasi-2D ( $500 \times 300 \times 28$ )



Movie S1. Movie of *Lumbriculus variegatus* burrowing through water-saturated soft sediment bed composed of transparent granular hydrogels in a container with  $H_c = 22.2$  cm,  $L_c = 21.5$  cm, and  $W_c = 1.27$  cm. The worm length is 36.6 mm. The movie corresponds to a 1000 second sequence recorded at 1 frames per second and played back at 5 frames per second. The movie corresponds to Fig. 1D.

Movie S2. Movie of *Lumbriculus variegatus* burrowing through water-saturated soft sediment bed composed of transparent granular hydrogels in a 2 mm wide container. The worm length is 26.6 mm. The movie corresponds to a 40 second sequence recorded at 5 frames per second and played back at 5 frames per second. The movie corresponds to Fig. 2A

Movie S3. Movie of *Lumbriculus variegatus* swimming in a water filled container. The worm length is 28 mm. The movie corresponds to a 40 second sequence recorded at 5 fps and played back at 5 fps. The movie corresponds to Fig. 2B.

Movie S4. A high speed movie of peristaltic motion observed along the body of a *Lumbriculus variegatus* swimming through water.

Movie S5. Movie of *Eisenia fetida* burrowing through water-saturated soft sediment bed composed of transparent granular hydrogels. The worm length is 68.6 mm. The movie corresponds to a 40 seconds sequence recorded at 4.5 fps and played back at 5 fps. The movie corresponds to Fig. 6A.



**Additional data table S1 (DatasetS1.xls)**

Excel file contains X and Y coordinate position of the tracked shape of *L. variegatus* shown in Fig. 1. The sheets are labeled according to the frame number at 1 frame per second.

**Additional data table S2 (DatasetS2.xls)**

Excel file contains X and Y coordinate position of the tracked shape of *L. variegatus* in sediments shown in Fig. 2. The sheets are labeled according to the frame number at 5 frame per second.

**Additional data table S3 (DatasetS3.xls)**

Excel file contains X and Y coordinate position of the tracked shape of *L. variegatus* in water shown in Fig. 2. The sheets are labeled according to the frame number at 5 frame per second.

**Additional data table S4 (DatasetS4.xls)**

Excel file contains X and Y coordinate position of the tracked shape of *E. fetida* in sediments shown in Fig. 6. The sheets are labeled according to the frame number at 5 frame per second.

**Additional data table S5 (DatasetS5.xls)**

Excel file listing worm number, run number, worm length, worm speed, transverse amplitude, transverse period, longitudinal amplitude, and longitudinal period for the two different species corresponding to data plotted in Figs 3,4,5.



## References

1. Doi M, Edwards SF (1988) *The Theory of Polymer Dynamics*. (Clarendon Press).
2. Panaitescu A, Clotet X, Kudrolli A (2017) Drag law for an intruder in granular sediments. *Physical Review E* 95:032901.
3. Allen B, Kudrolli A (2019) Effective drag of a rod in fluid-saturated granular beds. *Phys. Rev. E* 100:022901.
4. Jewel R, Panaitescu A, Kudrolli A (2018) Micromechanics of intruder motion in wet granular medium. *Physical Review Fluids* 3:084303.
5. Brodu N, Dijksman JA, Behringer RP (2015) Spanning the scales of granular materials through microscopic force imaging. *Nature Communications* 6:6361.
6. Andreotti B, Forterre Y, Pouliquen O (2013) *Granular Media Between Fluid and Solid*. (Cambridge University Press).
7. Drewes C, Cain K (1999) As the worm turns: Locomotion in a freshwater oligochaete worm. *The American Biology Teacher* 46:438–442.